Pergamon

PII: S0960-0779(96)00049-5

Fundamentals of Constructing Particle-Laden Jetflow by Fractal Point Sets and Predicting 3D Solid-Erosion Rates

Z. YONG and R. KOVACEVIC

Center for Robotics and Manufacturing Systems, University of Kentucky, Lexington, KY 40506-0108, USA

Abstract—A theoretical framework is established for constructing arbitrary particle-laden jetflow by means of fractal sets in the sense of average scale. This novel approach involves three main coherent components, in which one (1) searches for an appropriate original point set and confirms its intrinsic properties such as chaos, symmetry and density distribution; (2) derives governing equations for the formation of new point sets with any geometric configuration and desired normal velocity profile so that they can physically and geometrically represent particle motion on the cross-section of jetflow; and (3) develops the constitutive equations of particle–target interaction with erosion histories of particles and introduces the memory-element technique to handle the chaotic penetrating capabilities of millions of particles. Based on these results, the model is applied to predict the erosion rate in a drilling operation by abrasive waterjet. Results show that theory is consistent with experiments of drilling glass and titanium. © 1997 Elsevier Science Ltd All rights reserved

1. INTRODUCTION

Recently, the attention received by three-dimensional (3D) abrasive waterjet (AWJ) machining has led to an increase in both laboratory experimentation and usage in industrial practice. As a result, this state-of-the art cutting tool has been promoted to a multifunctional level, and is currently used for milling, drilling and turning hard-to-machine materials, such as titanium and advanced ceramics. Extensive research by engineers and scientists in diverse disciplines [1–11] has proved the 3D machining technique to be industrially applicable and to have some remarkable advantages in comparison with traditional tools. At present, however, the purely experiment-oriented research is facing great challenges in extending the knowledge from laboratories to the shop floor due to the lack of a theoretical basis behind 3D machining. This issue arises because many machining parameters, such as material properties, jet velocity and nozzle traverse rate, to name just a few, are coherently influential on the machining result. Consequently, the current research activities must rely heavily on numerous tentative tests on a case-by-case basis, making the achievements too specific for industrial applications. To reduce the cost and improve the quality of products, a model for off-line simulation becomes imperative.

Transported by high speed waterjet and air (600–900 m/s), about 10^5 tiny solid particles per second go through the cross-section of a nozzle (diameter 1.5–2.5 mm) and penetrate into the material to be machined. The machining result depends on the kinetic energy of each individual particle among the millions in the multiphase flow. Thus it is crucial for an accurate model to analyze the kinematic property of every particle.

It is a well-known fact that there have been great difficulties in coping with the turbulence of even a one-phase flow to date. Therefore from the point of view of fluid mechanics, it is not reasonable in a short term to expect to gain quickly a thorough understanding of the chaotic behavior of solid particles in a multiphase flow like AWJ. To

satisfy the requirements of modeling 3D machining by AWJ, a new approach is proposed to simulate particle-laden flow by means of fractal point sets with chaotic features. Once the jetflow is produced on the firm physical background, one can obtain the spatial positions and kinetic energy distribution of particles for evaluation of the erosion rate.

In addition, the constitutive equations of the particle–target interaction and the memory-element technique are developed in association with the generated flow to form a complete theoretical framework. The accuracy of the model for the drilling operation is satisfactorily verified by drilling experiments of glass and titanium.

2. CONSTRUCTION OF PARTICLE-LADEN JETFLOW

Subjected to physical and geometrical constraints, the particle motion should possess the following general features on the cross-section of multiphase particle-laden jetflow:

- The particle behavior is unpredictable.
- With the increase of time the particle distribution over the cross-section could be symmetrical or axisymmetrical if the density of particles is a constant or a symmetrical function and the shape of the cross-section is also symmetrical or axisymmetrical.
- The number of particles passing through the cross-section is instantly measurable since the particle flow-rate is measurable.
- The normal velocity of a particle varies with its position.

The particle motion will be simulated by fractal point sets derived from a Julia set through nonlinear iterations. For compactness, attention will not be focused on describing the fractal features of point sets but on their applications to the machining process. However, some obvious fractal phenomena will be still observed on the displayed figures.

2.1. *An original point set*

Under the coordinate system (x, y) or (r, θ), let $F_p = \{(\xi_1, \eta_1), (\xi_2, \eta_2), \ldots, (\xi_n, \eta_n)\}$ be a real point set produced by the nonlinear iterative equation

$$Z_{N+1} = \sqrt{(Z_N^2(Z_N - 1.24))} - 0.368 + 0.4436i \qquad (N = 1, 2, \ldots), \qquad (1)$$

where $Z_N = \xi_N + \eta_N i$ is a complex variable. Then a subset f_p of F_p is defined as the original point set, given by

$$f_p = \{(x_1, y_1), (x_2, y_2), \ldots, (x_n, y_n)\} = \{(r_1, \theta_1), (r_2, \theta_2), \ldots, (r_n, \theta_n)\} \subset F_p, \qquad (2)$$

where

$$0 \leqslant x_n^2 + y_n^2 = r_n^2 \leqslant 1, \qquad -\pi \leqslant \theta_n = \arctan(y_n/x_n) < \pi, \qquad (n = 1, 2, \ldots), \qquad (3)$$

$$x_n = 5\xi_N + 0.7, \qquad y_n = 5\eta_N - 1.5. \qquad (4)$$

The geometric configuration of f_p is displayed in Fig. 1. The moment t at which the nth particle appears on the circular domain is calculated from the equation

$$t = n/\dot{m} \qquad (5)$$

where $\dot{m}$ is the particle flow-rate. In most machining operations, $\dot{m}$ is a constant which is measured and controlled by an abrasive flow meter. From now on, the points of f_p are considered as the representation of particles on the circular cross-section of particle laden flow.

To examine properties of points, the cross-section of jetflow is divided into small
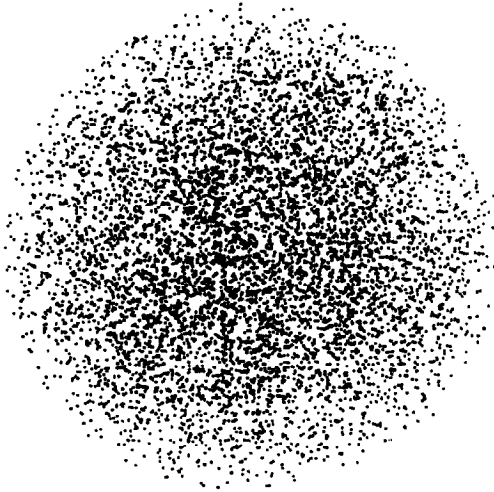
Fig. 1. Particle distribution of f_p.

elements under the polar coordinate system (r, θ), as shown in Fig. 2, and it is termed the net dish. The total number of elements L is determined by $L = KM$, where K is the number of divisions along the radial direction and M is the number of divisions along the circumferential direction. For instance, $K = 3$ and $M = 8$ lead to $L = 24$.

Because the existence and stability of important geometric and physical properties endowed to points of f_p later on are inherently relevant to the particle number n and the element number L in the net dish, the parameter α_p is introduced to measure this dependence. The form of α_p is

$$\alpha_p(L, n) = \frac{L}{n} \times 10^3. \tag{6}$$

In the practical situation, only $n \gg L$ is meaningful. In general, it is preferable that a desired property of f_p can hold for a relatively larger value of α_p.

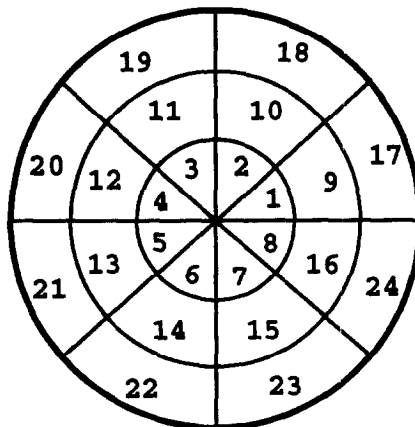An application of the net dish is to verify the chaotic appearance of particles. Under the

Fig. 2. The net dish with $K = 3$ and $M = 8$.

measurement $\alpha_p(4 \times 10^2, 10^4) = 40.0$, where $L = K \times M = 20 \times 20$, for instance, 16 parti-
cles are trapped in the 80-th element and their appearance orders in the element are listed
below:

$$\begin{pmatrix} 23 & 724 & 770 & 2032 \\ 2495 & 2714 & 3038 & 3481 \\ 3795 & 5214 & 6315 & 8345 \\ 8369 & 8889 & 8984 & 9547 \end{pmatrix}. \tag{7}$$

Obviously, no pattern exists to suggest that the particles of f_p follow any regular
movement. As a matter of fact, there are many alternative approaches which demonstrate
the chaotic behavior of the point appearance of f_p.

A function of the net dish is to examine the axisymmetrical characteristic of f_p. If $K = 1$
and M is an arbitrary integer, then every element of the net dish is wedge-shaped. Because
the number of particles in each element is approximately equal for a given n, the particle
distribution is confirmed to be highly axisymmetrical in a kinematic sense relevant to
$\alpha_p(L, n)$, as displayed in Fig. 3.

2.2. Governing equations

In the modeling of 3D machining, it is essential to find the velocity profile of a point set
along the normal direction of the cross-section. Before proceeding to the derivation of
governing equations, several assumptions are stated as follows:

- The solid particles in multiphase jetflow are uniformly mixed with the transportation
  mediums like water and air. This assumption will be proven true for f_p in Section 2.5.
- Only the average normal velocity profile is considered for turbulent flow since the
  erosion capacity of a particle depends on the kinetic energy of the normal direction.
- The sizes and shapes of particles are the same. In applications, particles are strictly
  categorized in terms of their average size, thus the influence of sizes should be less
  significant. The error caused by diverse shapes of particles is taken into account by
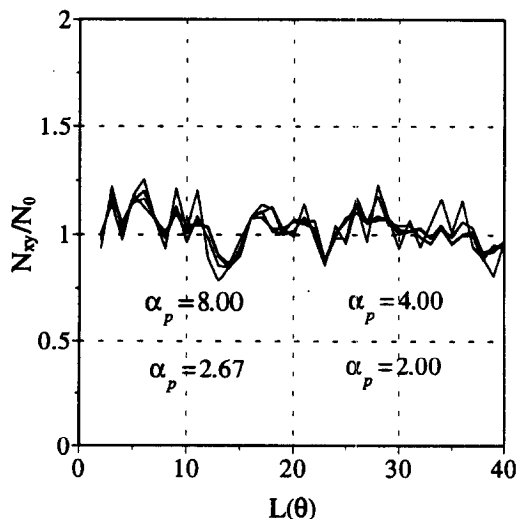 experimental parameters of constitutive equations.

Fig. 3. Demonstration of the axisymmetric property of f_p.

Based on the mass conservation principle associated with the above assumptions, one of the governing equations for determining the velocity profile is written in the form of a flow-rate ratio R_f:

$$\left(\int_{t_1}^{t} dt \iint_{S_{xy}} V_z \, ds\right)\bigg/\left(\int_{t_1}^{t_2} dt \iint_{S_0} V_z \, ds\right) = \frac{N_{xy}}{N_0} = R_f \qquad (t_1 \leq t \leq t_2). \tag{8}$$

In (8), $V_z = v_{zp}(t, x, y)/v_{max}$ $(0 \leq V_z \leq 1)$ is the dimensionless normal velocity profile of particles at the point (x, y) and instant t, v_z is the average normal velocity profile of particles and v_{max} is its maximum value, S_{xy} is an arbitrarily-shaped subarea of the cross-section S_0 of particle-laden jetflow, N_{xy} is the number of particles passing through S_{xy} in the time interval $t - t_1$ and N_0 is the number of particles passing through S_0 during $t_2 - t_1$. Obviously, the inequality $0 \leq R_f \leq 1$ holds.

It is necessary to point out that the border of the cross-section S_0 can have a general shape or consist of several independent boundaries rather than a single circle. For steady flow, (8) is reduced to

$$\left(\iint_{S_{xy}} V_z \, ds\right)\bigg/\left(\iint_{S_0} V_z \, ds\right) = \frac{N_{xy}}{N_0} = R_f. \tag{9}$$

From (8) V_z can be expressed by

$$V_z(t, x, y) = \left(\int_{t_1}^{t_2} dt \iint_{S_0} V_z \, ds\right)\frac{\partial^3 R_f}{\partial x \partial y \partial t} \tag{10}$$

under the Cartesian coordinates or

$$V_z(t, r, \theta) = \left(\int_{t_1}^{t_2} dt \iint_{S_0} V_z \, ds\right)\frac{1}{r}\frac{\partial^3 R_f}{\partial \theta \partial r \partial t} \tag{11}$$

under the polar coordinates. For steady flow, eqn (10) reduces to

$$V_z(x, y) = \left(\iint_{S_0} V_z \, ds\right)\frac{\partial^2 R_f}{\partial x \partial y} \tag{12}$$

and (11) becomes

$$V_z(r, \theta) = \left(\iint_{S_0} V_z \, ds\right)\frac{1}{r}\frac{\partial^2 R_f}{\partial \theta \partial r}. \tag{13}$$

In particular, for axisymmetric steady flow, eqn (13) is simplified to

$$V_z(r) = \left(\int_0^b V_z(r) r \, dr\right)\frac{1}{r}\frac{\partial R_f}{\partial r}, \tag{14}$$

where b is the radius of the nozzle. According to (9–14), a particle distribution on the cross-section corresponds to a velocity field through $R_f = N_{xy}/N_0$. Once the point set is given, the velocity is also determined in terms of R_f. It turns out that the central task for constructing a particle-laden jetflow is to find such a point set that possesses the desired velocity field. To avoid sophisticated mathematical treatments, the focus in the following parts is concentrated only on the steady jetflow.

2.3. Axisymmetric flow

As shown in Fig. 3, the particle distribution of f_p on the cross-section is very weakly dependent on the angle θ once α_p is smaller than a certain value. Therefore it can be reasonably treated as the representation of particle motion on the cross-section of steady

axisymmetrical particle-laden flow. Theoretically speaking, two key parameters R_f and V_z of f_p can be determined numerically by use of eqns (9) and (14). However, the modeling process could be impractical due to long computations resulting from the quantification of R_f and V_z.

To avoid these potential difficulties, approximate analytical expressions should be found for R_f and V_z of f_p. After computational experimentation, it is confirmed that

$$R_{fp} = 1 - (1 - r)^{11/10}[1 + (11/10)r], \tag{15}$$

$$V_{zp} = (1 - r)^{1/10} \tag{16}$$

are accurate for the replacement of R_f and V_z of f_p when $n > 5000$. A comparison between $V_z(r)$ and V_{zp}, $R_f(r)$ and R_{fp} is displayed in Fig. 4.

For applications, a question may arise: how can one find numerous new point sets to fit different velocity distributions appearing in the practical situations? The strategy in this work is to utilize mapping techniques to convert f_p into a new point set.

The well-known analytical result of V_f for one-phase flow is used in order to minimize computational burden for multiphase steady flow. That is, for laminar flow the dimensionless velocity V_z^l is written as [12]

$$V_z^l(r) = 1 - r^2 \qquad (0 \leqslant r \leqslant 1) \tag{17}$$

and for turbulent flow the average velocity profile V_z^t is described by the seventh-root law [12]

$$V_z^t(r) = (1 - r)^{1/7} \qquad (0 \leqslant r \leqslant 1). \tag{18}$$

Substitution of (17) and (18) into (9) leads to the flow-rate ratios

$$R_f^l = r^2(2 - r^2), \tag{19}$$

$$R_f^t = 1 - (1 - r)^{8/7}[1 + (8/7)r], \tag{20}$$

respectively. There are two steps in mapping f_p onto a new point set, denoted by $f_p^M = \{(\zeta_1, \theta_1), (\zeta_2, \theta_2), \ldots, (\zeta_k, \theta_k)\}$. First, calculate the flow-rate $R_f(\zeta)$ in terms of the given velocity V_z such as V_z^l and V_z^t. Secondly, for a point $(r_n, \theta) \in f_p$, find a root ζ_n by equating $R_{fp}(r_n)$ of f_p to $R_f^l(\zeta_n)$ or $R_f^t(\zeta_n)$, which generates a point $(\zeta_n, \theta_n) \in f_p^M$.
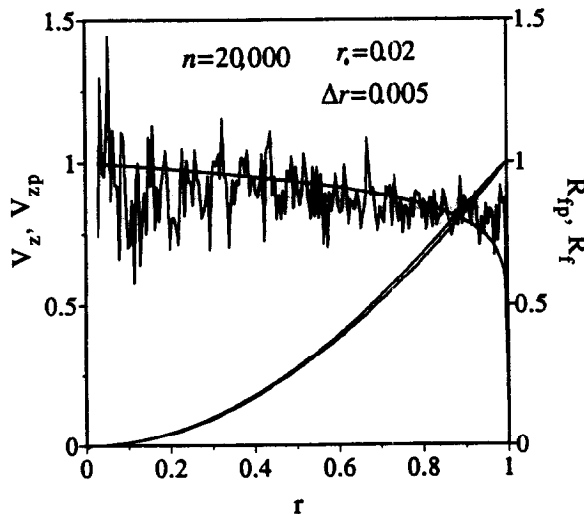

Fig. 4. V_z and V_{zp}, R_f and R_{fp} of f_p.

Repeating the one-to-one and onto mapping for different r_k yields the new point set with the desired velocity profile and flow-rate ratio. Note that the mapping takes place only between two radial variables r_n and ζ_n, and the angles θ_n are equal because of the axi-symmetrical nature.

Following the two guidelines, the equation for determining points ζ_k for laminar flow is

$$R_f^l = R_{fp} \rightarrow \zeta_k = \sqrt{(1 - \sqrt{((1 - r_k)^{11/10}(1 + (11/10)r_k)))}}. \tag{21}$$

and similarly ζ_k for turbulent flow are calculated by

$$R_f^t = R_{fp} \rightarrow (1 - \zeta_k)^{8/7}[1 + (8/7)\zeta_k] = (1 - r_k)^{11/10}[1 + (11/10)r_k]. \tag{22}$$

After the new point set f_p^M is produced, it is an important step to check R_f and V_z of f_p^M by using equations $R_f = N_{xy}/N_0$ and $V_z = [R_f(\zeta_{k+1}) - R_f(\zeta_k)]/[\zeta_{k+1}(\zeta_{k+1} - \zeta_k)]$, so as to prevent the potential errors from numerical treatments.

2.4. Non-axisymmetric jetflow

Mapping the original set f_p into a non-axisymmetrical set is a much more complicated task because, generally speaking, both the geometrical and physical features of f_p will be completely reshaped through the transformation. In this circumstance, a mathematical approach is effective mostly on a case-by-case basis. For brevity, a detailed description is given here to explain how to generate a point set with the elliptic shape and the velocity of laminar flow.

Under the Cartesian and polar coordinates, the dimensionless velocity profile in eqn (9) is assumed to be the same for an elliptic steady laminar flow [13], given by

$$V_z^e = 1 - \frac{x^2}{a^2} - \frac{y^2}{b^2} = 1 - r^2\left(\frac{\cos^2 \theta}{a^2} + \frac{\sin^2 \theta}{b^2}\right), \tag{23}$$

where a and b are the major and minor semiaxes of the ellipse, respectively. After substitution of (23) into (9), lengthy calculations result in

$$\iint_{S_{xy}} V_z^e \, ds = \int_0^\phi d\theta \int_0^{\rho_\theta}\left[1 - r^2\left(\frac{\cos^2 \theta}{a^2} + \frac{\sin^2 \theta}{b^2}\right)\right] r \, dr = \frac{ab}{4}\sigma^2(2 - \sigma^2)\arctan\left(\frac{a}{b}\tan\phi\right), \tag{24}$$

$$\iint_{S_0} V_z \, ds = \left(\iint_{S_{xy}} V_z \, ds\right)_{\substack{\sigma=1 \\ \phi=2\pi}} = 2\pi\frac{ab}{4}, \tag{25}$$

with

$$\rho_\theta = \frac{\sigma}{\sqrt{((\cos^2 \theta)/a^2 + (\sin^2 \theta)/b^2)}}, \qquad 0 \leqslant \sigma = \frac{a_x}{a} = \frac{b_x}{b} \leqslant 1, \tag{26}$$

where a_x and b_x are the major and minor semiaxes of a smaller ellipse which is similar to the border of the cross-section. From eqns (24) and (25), one can obtain the flow-rate ratio R_f^e for the elliptic cross-section

$$R_f^e = \frac{1}{2\pi}\sigma^2(2 - \sigma^2)\arctan\left(\frac{b}{a}\tan\phi\right). \tag{27}$$

Additionally, when the polar angle θ is taken into account in eqn (16) R_{fp} can be rewritten as

$$R_{fp} = \frac{\theta}{2\pi}\{1 - (1 - r)^{11/10}[1 + (11/10)r]\}. \tag{28}$$

Letting $R_f^e = R_{fp}$, one can find two mapping equations for a new point set $f_p^M = \{(\zeta_1, \phi_1),$ $(\zeta_2, \phi_2), \ldots, (\zeta_k, \phi_k)\}$ in the forms

$$\arctan\left(\frac{a}{b}\tan\phi_k\right) = \theta_k \rightarrow \tan\phi_k = \frac{b}{a}\tan\theta_k \qquad (k = 1, 2, \ldots, n) \qquad (29)$$

and

$$\sigma_k = \sqrt{(1 - \sqrt{((1 - r_k)^{11/10}(1 + (11/10)r_k)))} \rightarrow \zeta_k = \frac{\sigma_k b}{\sqrt{(1 - (1 - b^2/a^2)\cos^2\phi_k)}}. \qquad (30)$$

The new set f_p^M is the representation of particle motion on the elliptic cross-section of laminar particle-laden flow; an example is shown in Fig. 5. The comparison between numerical and analytical results of R_f^e and V_z^e is now given here for briefness.

There is no analytical expression for turbulent flow in the elliptic nozzle. By analogy with the seventh-power law [12], the dimensionless velocity profile in this case is assumed to have the form

$$V_z = \left(1 - \sqrt{\left(\frac{x^2}{a^2} + \frac{y^2}{b^2}\right)}\right)^{1/7} = \left(1 - r\sqrt{\left(\frac{\cos^2\theta}{a^2} + \frac{\sin^2\theta}{b^2}\right)}\right)^{1/7} \qquad (31)$$

which is consistent with the meaning of the axisymmetrical case on $x = 0$ and $y = 0$. After tedious calculations, the mapping functions are given by

$$\tan\phi_k = \frac{b}{a}\tan\theta_k, \qquad (32)$$

$$(1 - \sigma_k)^{8/7}[1 + (8/7)\sigma_k] = (1 - r_k)^{11/10}[1 + (11/10)r_k] \rightarrow \zeta_k$$

$$= \frac{\sigma_k b}{\sqrt{(1 - (1 - b^2/a^2)\cos^2\phi_k)}}. \qquad (33)$$

for a new point set.

It turns out from the above analyses that two mapping equations are necessary to generate an elliptic point set from the original set. One is related to the angular variable
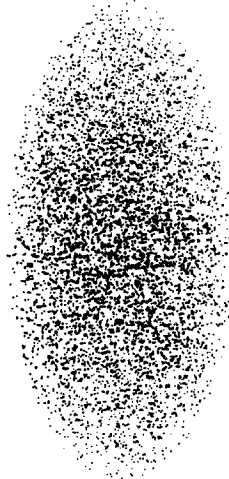

Fig. 5. Particle distribution ($n = 3000$) on the elliptic cross-section.

and the other to the radius. In the above discussions the two mapping equations are noncoupled so that points (ζ_k, ϕ_k) can be ascertained directly. This type of advantage may not exist for those problems which have the mapping variables coupled together.

2.5. *Verification of constant density*

During derivations of governing equations, the density of particles is assumed to be a constant at any instant when n exceeds a certain number. Next it will be verified that this assumption holds for the point set f_p.

The density ρ is defined as the ratio

$$\rho = \frac{M_p}{V_d} = \frac{m_p N_{xy}}{\int_{t_1}^{t_2} dt \iint_{S_{xy}} V_z \, ds}.$$ (34)

In equation (34), $M_p = m_p N_{xy}$ is the total mass of N_{xy} particles, where m_p is the average mass of particles, V_d is the volume of multiphase flow passing through S_{xy} during $t_2 - t_1$. For steady flow, based on $\dot{m} = N_0/(t_2 - t_1)$ and $\bar{V}_z = \iint_{S_{xy}} V_z \, ds/S_{xy}$, where $\bar{V}_z$ is the average value of V_z in the subdomain $S_{xy} \subset S_0$, eqn (34) is reduced to

$$\rho = \frac{m_p \dot{m}}{S_{xy} \bar{V}_z} \frac{N_{xy}}{N_0}.$$ (35)

Note that m_p and $\dot{m}$ are constants and so it is sufficient to verify that $\rho/(m_p \dot{m})$ is a constant. Again, the net dish shown in Fig. 2 is employed to identify the correctness of (35). In this circumstance, S_{xy} is the area of an element, N_{xy} is the number of particles passing through S_{xy} and $\bar{V}_z$ is evaluated by the velocity of the geometric center of S_{xy}.

The numerical results for the original point set f_p are shown in Fig. 6 by means of $\rho/(m_p \dot{m})$ vs $L = KM$. Excluding the small zone near the center ($r = 0$) of the cross-section, ρ as defined by (35) can be taken as a constant if the negligible oscillations around the constant are disregarded. Examinations confirm that the large error appearing near the center does not have any significant influence on either application or theoretical correctness because the error is caused mainly by the small value of the wedge-shaped areas $S_{xy} = r^2\theta/2$ near the center. When $r \to 0$, S_{xy} becomes very small and eqn (35)
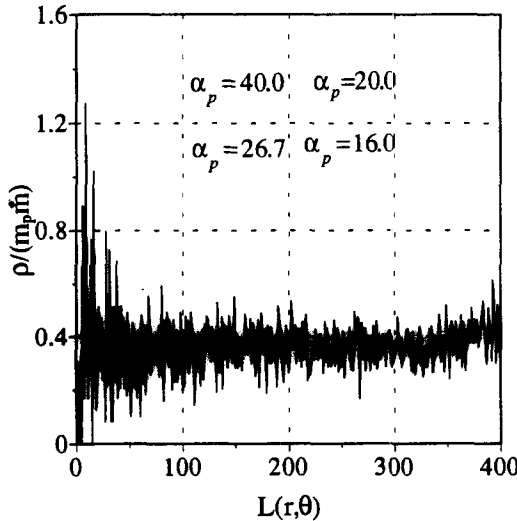

Fig. 6. Demonstration of the uniform density of f_p.

approaches singularity. As a result the density appears to oscillate sharply. A similar analysis is also feasible for any new point set if required.

3. PREDICTION OF DEPTH OF DRILLING

With the aid of the suitable point sets tó represent moving particles, this section focuses on the simulation of drilling a hole by abrasive waterjet.

In dealing with this seemingly simple problem, researchers and engineers are actually facing one of the most challenging topics in abrasive waterjet machining. For a rational model, at least two essential issues are unavoidable. First, the model should consider the diminution of penetrating abilities of particles with increasing the depth of drilling. Secondly, erosion or wear mechanisms of different materials by particle impact should be reflected in the model. The first issue requires the model to consider erosion histories of all particles. In addition, parameters like intensities of inflow and outflow during the formation of a hole could also be influential in various machining environments.

3.1. *Constitutive equations*

No matter how many parameters are involved in a drilling process, the penetrating ability of a single particle depends on the constitutive equation of the particle–target interaction. In the past three decades, many models for predicting the average erosion rate by particle impact (e.g. [14–16]) have been presented and can be summarized by the unified equation

$$\delta h_j = \lambda_1 [V_z(x_{\alpha_i}, y_{\alpha_i})]^{\lambda_2}. \tag{36}$$

In equation (36), δh_j is the average height of a fragment or a chip removed by the jth particle striking the small area centered at $(x_{\alpha_i}, y_{\alpha_i})$ on the workpiece, λ_1 and λ_2 are physical constants which include the effects of material properties, the impact angle and shape of a particle and target, and so on.

In order to develop a suitable model applicable to the shop floor, a strategy is adopted to modify (36) so that its applicable scope can be extended to a deeper drilling operation. The form of (36) is retained but λ_1 and λ_2 are taken as functions of the cutting depth h. That is,

$$\delta h_j = \lambda_1(h_{j-1})[V_z(x_{\alpha_i}, y_{\alpha_i})]^{\lambda_2(h_{j-1})}, \qquad (j = 1, 2, \ldots, n) \tag{37}$$

where h_{j-1} is the average depth of cut produced by $j - 1$ particles previously striking a very small region around the point $(x_{\alpha_i}, y_{\alpha_i})$ and at instant $t_j = j/\dot{m}$. Note that $h_j = h_{j-1} + \delta h_j$ and

$$h_j = \sum_{k=1}^{j} \delta h_k = \sum_{k=1}^{j} \lambda_1(h_{k-1})[V_z(x_{\alpha_i}, y_{\alpha_i})]^{\lambda_2(h_{k-1})}. \tag{38}$$

This equation suggests that the erosion rate of a particle depends on the histories of other particles prior to it.

It is important to point out that the values of λ_1 and λ_2 are not arbitrary but controlled by certain physical principles like energy conservation. A constraint on λ_2 for brittle erosion is derived as the illustration of this statement. In such a circumstance, the material removal is considered to be a result of brittle fragmentation [17, 18]. Without loss of generality, the new surface created by a particle is assumed to be equal to $S_f(\delta h_j)^2$, where S_f stands for a geometrically transforming constant. As a result, the surface energy E_s

consumed by the new surface is expressed as $E_s = \gamma_0 S_f(\delta h_j)^2$, where γ_0 is the surface energy density.

Multiplying eqn (37) by $S_f\gamma_0\delta h_j$ leads to

$$E_s = S_f\gamma_0(\delta h_j)^2 = S_f\gamma_0[\lambda_1(h_{j-1})]^2[V_z(x_{\alpha_i}, y_{\alpha_i})]^{2\lambda_2(h_j-1)} < \tfrac{1}{2}m_p[V_z(x_{\alpha_i}, y_{\alpha_i})]^2. \qquad (39)$$

The physical meaning of eqn (39) is that the surface energy consumed by fragmentation is less than the total kinetic energy of the particle. Furthermore, the inequality of (39) can be rewritten as

$$\lambda_1^2 V_z^{2(\lambda_2-1)} < \frac{m_p}{2S_f\gamma_0}. \qquad (40)$$

Theoretically speaking, λ_1 and λ_2 are independent of V_z. Therefore, to have a bounded value on the left-hand side of (40), the inequality $\lambda_2 \geqslant 1$ must hold. Otherwise, when V_z is smaller this inequality from the energy conservation principle would not hold. For ductile materials, theoretical and experimental analyses show that λ_2 varies between 2 and 2.3 [14–16], and it is consistent with the physical meaning.

For the modeling of drilling, the explicit forms of λ_1 and λ_2 are chosen such that they can reflect the influence of the damping and other effects like the resistance of outflow. In this work they are of the form

$$\lambda_1 = \frac{l_0}{h_{j-1}^{l_1} + 1}, \qquad (41)$$

$$\lambda_2 = l_2 h_{j-1} + 2, \qquad (42)$$

where l_i $(i = 0, 1, 2)$ are constants determined by experiments. Substitution of (41) and (42) into (37) yields

$$\delta h_j = \frac{l_0}{h_{j-1}^{l_1} + 1}[V_z(x_{\alpha_i}, y_{\alpha_i})]^{l_2 h_{j-1}+2}. \qquad (43)$$

This equation is consistent with the classical one when $l_1 = l_2 = 0$. It follows from (43) that the erosion rate decreases when the depth of drilling increases and the shape of the hole is also changed since the dimensionless velocity $V_z(x_{\alpha_i}, y_{\alpha_i}) \leqslant 1$ is associated with exponent $l_2 h_{j-1} + 2$.

3.2. Modeling of drilling

Determining how many particles strike a given small area is the primary step in calculating the depth of drilling at that area. Usually the chaotic motion or unpredictable manner of particles can bring about great difficulties to tracing trajectories of particles. Nevertheless, the point set f_p^M obtained previously makes the task feasible. The following introduces a new approach for recording histories of individual particles.

The net dish in Fig. 2 is now applied to the surface to be drilled. Every element of the dish acts as a memory cell to trap every particle falling into it. The average depth generated by a particle, say the jth particle, in the cell corresponds to δh_j of eqn (37) in which the coordinates $(x_{\alpha_i}, y_{\alpha_i})$ are defined as the center of the cell. For axisymmetrical laminar flow, V_z is given by eqn (17), and then eqn (43) becomes

$$\delta h_j = \frac{l_0}{h_{j-1}^{l_1} + 1}(1 - r_i^2)^{l_2 h_{j-1}+2} \qquad (r_i = \sqrt{(x_{\alpha_i}^2 + y_{\alpha_i}^2)}) \qquad (44)$$

and for turbulent flow, from the average velocity profile given by (18) one obtains

$$\delta h_j = \frac{l_0}{h_{j-1}^{l_1} + 1}(1 - r_i)^{(l_2 h_{j-1} + 2)/7} \qquad (r_i = \sqrt{(x_{\alpha_i}^2 + y_{\alpha_i}^2)}). \tag{45}$$

The final depth of drilling in each element is the accumulation of erosion of all the particles. The three-dimensional drilling profile of a hole forms after the depth of every element in the drilling region is available. The detailed numerical treatment is not described here due to sophisticated procedures. Two examples are displayed in Fig. 7 for 3D characteristics of two holes. One is for the case of laminar flow and the other is for the turbulent flow. Both the theoretical and experimental results show that $l_1 = 2.0$ holds for either brittle or ductile materials. In addition, $l_2 = 0.2$ appears to match the experimental shape of a hole. Clearly, the velocity profile has a very significant influence on the geometry of holes.

3.3. *Experiments*

The VISTA glass brick with the dimensions $8 \times 8 \times 3$ in³ is chosen as the specimen of a brittle material. Since waterjet pressure is as low as 50 MPa for drilling the glass brick, the abrasive waterjet is assumed to be laminar flow and hence the point set generated by (21) is the particle source of the modeling. The erosion rate is calculated by eqn (44). The comparison between theoretical and experimental analyses is listed in Table 1.

The specimen of the ductile material is made of titanium. Since the water pressure is as high as 240 MPa, the flow in this case can be verified as turbulent. The points derived from (22) are used to simulate the particle motion and the penetration abilities of them are evaluated by use of (45). Table 2 shows that theory is in good agreement with the experiments.
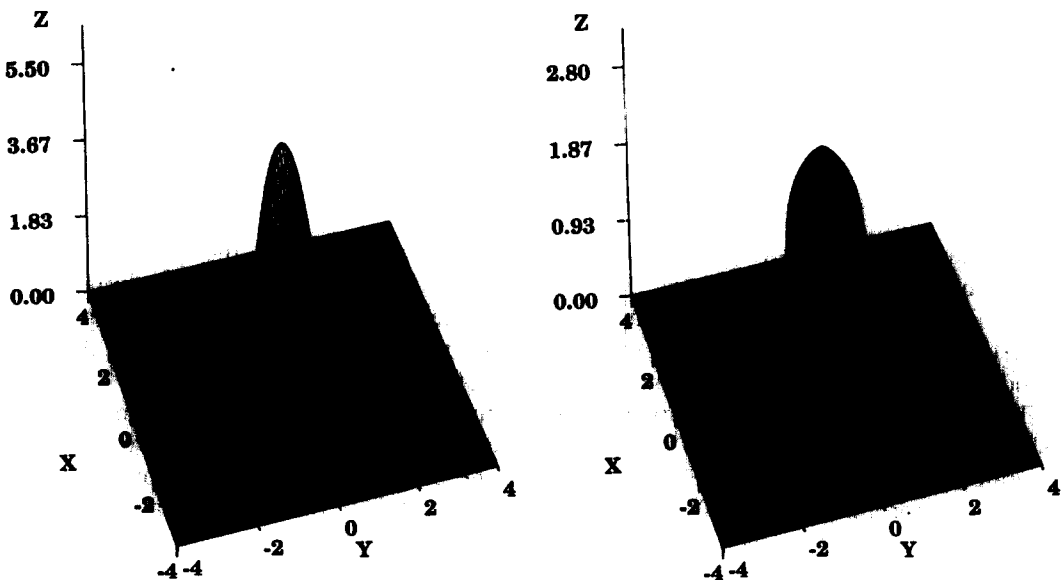

Fig. 7. Three-dimensional shape of a hole by (a) laminar and (b) turbulent flow.

Table 1. Comparison between theory and experiment for drilling glass

t	(s)	30	40	60	90
h_e	(mm)	33	40	46	55
h_t	(mm)	35.5	40.1	47.1	55.0

workpiece material: glass	waterjet pressure: 50 MPa
abrasive material: aluminium oxide	abrasive flow-rate: 5.4 g/s
size of abrasives: 100 (mesh)	standoff distance: 25 mm
diameter of mixing tube: 2.5 mm	$l_0 = 18.86$, $l_1 = 2.0$, $l_2 = 0.2$

Table 2. Comparison between theory and experiment for drilling titanium

t	(s)	12	21	40	60
h_e	(mm)	13	17	24	28
h_t	(mm)	14.4	18.5	23.5	28.0

workpiece material: titanium	waterjet pressure: 240 MPa
abrasive material: aluminium oxide	abrasive flow-rate: 5.4 g/s
size of abrasives: 100 (mesh)	standoff distance: 25 mm
diameter of mixing tube: 2.5 mm	$l_0 = 9.63$, $l_1 = 2.0$, $l_2 = 0.2$

4. CONCLUSION AND DISCUSSION

Constructing particle-laden flow by fractal point sets proves to be an effective approach to simulating three-dimensional drilling by abrasive waterjet. The most remarkable advantage of this method is that one finds an ideal particle source without extremely complex computation based on the many nonlinear partial differential equations in fluid mechanics or expensive and time-consuming experiments. The reason for the benefit is that a point set or particle source itself already carries chaotic behavior so that the procedure of obtaining the property is avoided.

The AWJ drilling operation is modeled in the present research and satisfactory results are achieved according to the agreement between the theory and experiment. For future work, many issues are still open for further research, such as the characterization of surface quality, non-steady flow simulation, and the fractal property of point sets.

REFERENCES

1. I. Finnie, The mechanisms of erosion of ductile metals. *Proceedings of the Third National Congress of Applied Mechanics*, ASME, 527–532 (1958).
2. J. G. A. Bitter, A study of erosion phenomena: Part I. *Wear* 6, 5–21 (1963).
3. J. G. A. Bitter, A study of erosion phenomena: Part II. *Wear* 6, 169–190 (1963).
4. A. G. Evans, M. E. Gulden and M. Rosenblatt, Impact damage in brittle materials in the elastic–plastic response regime. *Proc. R. Soc. A* 361, 343–365 (1978).
5. S. K. Li, J. A. C. Humphrey and A. V. Levy, Erosive wear of ductile metals by a particle-laden high velocity liquid jet. *Wear* 73, 295–309 (1981).
6. M. Hashish, Turning with abrasive waterjets – a first investigation. *ASME J. Engng. Ind.* 109, 281–290 (1987).
7. M. Hashish, An investigation of milling with abrasive waterjet. *ASME J. Engng. Ind.* 111, 158–166 (1989).
8. M. Hashish, Three-dimensional machining with abrasive waterjets. *Jet Cutting Technol.* 13, 605–620 (1992).

9. R. Kovacevic, Monitoring of depth of abrasive waterjet penetration. *Int. J. Mach. Tools Manufac.* **1**, 55–72 (1992).

10. J. Zeng and T. J. Kim, Development of an abrasive waterjet kerf cutting model for brittle materials. *Jet Cutting Technol.* **13**, 483–501 (1992).

11. S. P. Raju and M. Ramulu, Predicting hydro-abrasive wear during abrasive waterjet cutting – Parts I and II. *Seventh American Waterjet Conference*, Seattle, Washington (1993).

12. I. H. Shames, *Mechanics of Fluid*. McGraw-Hill, New York (1962).

13. I. G. Currie, *Fundamental Mechanics of Fluid*. McGraw-Hill, New York (1993).

14. I. Finnie, Erosion of surfaces by solid particles. *Wear* **3**, 87–103 (1960).

15. G. P. Tilly and W. Sage, The interaction of particles and material behavior in erosion process. *Wear* **16**, 447–465 (1970).

16. M. Hashish, A modeling study of metal cutting with abrasive waterjets. *ASME J. Engng Ind.* **106**, 88–100 (1984).

17. Z. Yong, M. T. Hanson and R. Kovacevic, Topological measure of brittle fragmentation. *Int. J. Solids Struct.* **31**, 391–415 (1994).

18. Z. Yong and R. Kovacevic, Simulation of chaotic motion of particles in jetflow and application to modeling abrasive waterjet machining. Accepted for publication by *ASME J. Fluid Engng* (accepted).